nature photonics

ARTICLES

PUBLISHED ONLINE: 2 MARCH 2015 | DOI: 10.1038/NPHOTON.2015.22

Deep *in vivo* photoacoustic imaging of mammalian tissues using a tyrosinase-based genetic reporter

Amit P. Jathoul[1,2‡], Jan Laufer[3,4†‡], Olumide Ogunlade[3], Bradley Treeby[3], Ben Cox[3], Edward Zhang[3], Peter Johnson[2,5], Arnold R. Pizzey[1,2], Brian Philip[1,2], Teresa Marafioti[6], Mark F. Lythgoe[5], R. Barbara Pedley[2], Martin A. Pule[1,2‡] and Paul Beard[3*‡]

Photoacoustic imaging allows absorption-based high-resolution spectroscopic *in vivo* imaging at a depth beyond that of optical microscopy. Until recently, photoacoustic imaging has largely been restricted to visualizing the vasculature through endogenous haemoglobin contrast, with most non-vascularized tissues remaining invisible unless exogenous contrast agents are administered. Genetically encodable photoacoustic contrast is attractive as it allows selective labelling of cells, permitting studies of, for example, specific genetic expression, cell growth or more complex biological behaviours *in vivo*. In this study we report a novel photoacoustic imaging scanner and a tyrosinase-based reporter system that causes human cell lines to synthesize the absorbing pigment eumelanin, thus providing strong photoacoustic contrast. Detailed three-dimensional images of xenografts formed of tyrosinase-expressing cells implanted in mice are obtained *in vivo* to depths approaching 10 mm with a spatial resolution below 100 μm. This scheme is a powerful tool for studying cellular and genetic processes in deep mammalian tissues.

Optical techniques such as fluorescence or bioluminescence imaging are widely used to visualize biological tissues *in vivo*[1–4]. However, strong optical scattering fundamentally limits the penetration depth or spatial resolution. Microscopy and other techniques that utilize ballistic photons[4] can provide cellular resolution, but only to sub-millimetre penetration depths, while diffuse optical methods such as fluorescence optical tomography[1] can provide greater penetration depths (on the scale of centimetres) but with only limited spatial resolution (on the scale of millimetres). Photoacoustic imaging (PAI) offers the prospect of overcoming these limitations[5–8]. Here, ultrasound waves generated by the absorption of laser light by tissue chromophores are used to produce images of biological tissues based on optical absorption. Because acoustic waves are scattered much less than photons in soft tissues, PAI avoids the depth and spatial resolution limitations of purely optical imaging techniques: depths of a few centimetres with scalable spatial resolution ranging from tens to hundreds of micrometres (depending on depth) are readily achievable.

Although strong absorption by haemoglobin enables the acquisition of exquisite three-dimensional photoacoustic (PA) images of the vasculature[9–14], most cells and tissues are relatively weakly absorbing at visible and near-infrared wavelengths and are thus indistinguishable in the absence of exogenous contrast. The latter can be provided by nanoparticle- or dye-based targeted contrast agents[15–17], but these can present challenges in achieving effective specific targeting and clearance. The use of reporter genes to provide genetically encoded exogenous PA contrast would avoid these limitations and has the further advantage of providing opportunities to study more complex biological behaviours such as cell growth dynamics and intracellular processes such as gene expression and signalling.

Several commonly used genetically expressed fluorescent proteins[18] have been shown to provide genetically encoded PA contrast but only in the relatively transparent zebrafish or small-scale *Drosophila* (fruitfly) pupa[19]. Most fluorescent proteins are not ideally suited as PA genetic reporters in more strongly attenuating mammalian tissues. This is because of their low extinction coefficients, poor PA generation efficiency and a paucity of photostable variants with sufficiently redshifted absorption beyond 650 nm to avoid that of haemoglobin[20]. The near-infrared fluorescent protein family (iRFP) provide an exception by exhibiting absorption in the 650–720 nm range[21,22]. However the use of these proteins can be complicated by the need for the non-ubiquitous pigment biliverdin for their biosynthesis. Genetically encoded enzymatic means of generating PA contrast have also been explored[23], with the transgenic expression of tyrosinase (Tyr) offering most promise. Tyr catalyses the formation of the pigment eumelanin from cellular tyrosine[24]. This pigment has strong broadband optical absorption, extending to wavelengths beyond that of haemoglobin, and exhibits high photostability. Several preliminary studies have explored the use of Tyr to generate PAI contrast[25–30]. However, *in vivo* image contrast has been modest for those studies that employed the deep tissue tomography mode of PAI[28–30]. Moreover, serial *in vivo* longitudinal studies, which are key to demonstrating stable transduction and biocompatibility, have not been reported. Both are essential prerequisites if Tyr-based genetic reporters are to find widespread practical application in the study of dynamic biological processes such as cell growth where repeated imaging of the same organism, over long periods, is required.

Here, we extend the use of Tyr in PAI using a novel retroviral vector co-expressing Tyr with a convenient surface marker gene, which allows engineering of cell lines to permanently express this

[1]Department of Haematology, University College London, Gower Street, London WC1E 6BT, UK. [2]Cancer Institute, University College London, Gower Street, London WC1E 6BT, UK. [3]Department of Medical Physics & Biomedical Engineering, University College London, Gower Street, London WC1E 6BT, UK. [4]Institut für Radiologie, Charité-Universitätsmedizin Berlin, Charitéplatz 1, Berlin 10117, Germany. [5]UCL Centre for Advanced Biomedical Imaging, University College London, Gower Street, London WC1E 6BT, UK. [6]Department of Pathology, University College London, Gower Street, London WC1E 6BT, UK; [†]Present address: Institut für Optik und Atomare Physik, Technische Universität Berlin, Strasse des 17. Juni 135, Berlin 10623, Germany. [‡]These authors contributed equally to this work. *e-mail: paul.beard@ucl.ac.uk

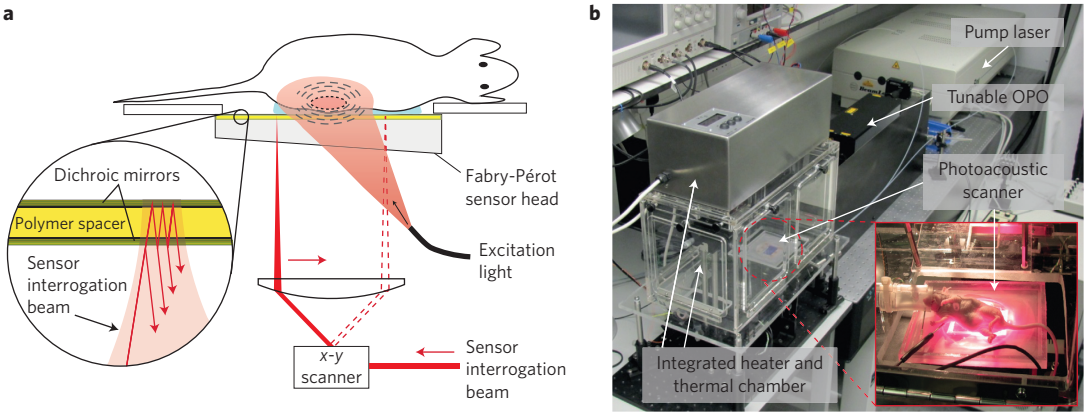

Figure 1 | Photoacoustic (PA) scanner for imaging mice *in vivo*. a, Schematic illustrating the scanner in operation. PA waves are generated by the absorption of nanosecond optical pulses provided by a fibre-coupled wavelength-tunable optical parametric oscillator (OPO)-based excitation laser system and detected by a Fabry–Pérot (FP) polymer film etalon ultrasound sensor. The excitation beam incident on the skin is ~2 cm in diameter. The sensor comprises a pair of mirrors separated by a 40-μm-thick polymer spacer, thus forming a FP etalon as illustrated in the inset. The etalon mirrors are dichroic: highly reflective in the sensor interrogation wavelength range (1,500–1,600 nm) but transparent to the excitation laser wavelengths used (typically 600–900 nm). This allows the excitation laser beam to be transmitted through the sensor head, enabling backward mode imaging. The incident PA waves are mapped in two dimensions by scanning the interrogation laser beam across the sensor surface and recording the acoustically induced modulation of the reflectivity of the etalon at each scan point. **b**, The system in operation, showing the anaesthetized animal located on the FP sensor head, through which the excitation laser pulses are delivered. An aqueous gel inserted between the skin and the sensor was used to provide acoustic coupling. All *in vivo* experiments were conducted without signal averaging and using an incident laser fluence below the safe MPE for human skin[37].

enzyme, and an imaging system based on a unique highly sensitive Fabry–Pérot (FP)-based optical ultrasound detector[10,31]. We show that this new approach allows Tyr-expressing mammalian cells to be selectively and unambiguously discriminated from the microvasculature with unprecedented contrast and penetration depth. Furthermore, unlike previous approaches, the use of a retroviral vector provides stable transduction; in other words, the genome is permanently altered so its progeny inherits the new modified gene. Image contrast is therefore passed on to progeny cells, allowing the visualization of cell population growth and other dynamic behaviour. We demonstrate this by imaging the growth of an expanding population of Tyr-expressing cells *in vivo* over extended periods in mice for the first time, by using PAI. The combination of high image contrast and stable transduction achieved in this study represents an important step towards the practical biological application of Tyr-based PA genetic reporters for cell tracking and other spatial-temporal monitoring studies of biological processes.

Fabry–Pérot etalon sensor-based PAI scanner. Unlike most PAI systems, which use conventional piezoelectric receivers to record the PA waves, the scanner used in this study employs an all-optical ultrasound detector based on a high finesse FP polymer film etalon. This approach offers several advantages, particularly in relation to acoustic performance, resulting in improved image quality compared to conventional piezoelectric implementations.

Figure 1 presents a schematic of the system. The FP imaging head consists of the sensing etalon overlaying a 10-mm-thick wedged polymethyl methacrylate (PMMA) backing substrate. The etalon is a thin-film structure comprising a 40-μm-thick Parylene C polymer spacer sandwiched between a pair of dichroic dielectric mirrors. The etalon was fabricated using all-vacuum deposition methods. The polymer spacer was formed by chemical vapour deposition, which provided the high thickness uniformity and surface quality required to achieve a high-finesse etalon, and the dichroic mirrors were deposited by ion-assisted sputtering. A key design feature is that the dichroic mirrors are only highly reflective in the 1,500–1,600 nm spectral range. At shorter wavelengths (600–1,200 nm) they are transparent. Excitation laser pulses in this latter spectral range can therefore be transmitted directly through the FP sensor head into the underlying tissue, thereby permitting convenient backward mode operation. Following absorption of the excitation laser energy in the tissue, PA waves are generated. These waves arrive at the etalon and modulate its optical thickness, which is detected using a continuous-wave 1,500–1,600 nm interrogation laser beam focused onto the etalon surface. To provide maximum sensitivity and linearity, the interrogation laser wavelength is tuned to the peak derivative of the etalon reflectance transfer function. Under these conditions the sensor is said to be optimally biased, and small acoustically induced changes in the etalon optical thickness are linearly converted to a corresponding temporal modulation of the reflected optical power. To map the spatial distribution of the incident PA waves, the interrogation beam is optically scanned point by point (one point per excitation laser pulse) over the surface of the etalon, and the time-resolved PA signals are recorded at each point. To compensate for variations in the optical thickness of the etalon spacer, the bias wavelength is optimally set at each scan point.

The transparent nature of the sensor head is clearly advantageous in terms of irradiating the tissue in that it avoids the challenges associated with delivering the excitation light around an opaque piezoelectric planar detector array. However, perhaps the most important advantage of this type of sensor derives from its exceptional acoustic performance in terms of bandwidth, element size and sensitivity. The well-matched acoustic impedances of the PMMA backing substrate and the polymer etalon spacer result in a near-uniform non-resonant broadband frequency response from 350 kHz to 22 MHz (−3 dB points)[31], a crucial requirement given the very broadband nature of PA waves produced by nanosecond pulsed excitation. Moreover, for an accurate image reconstruction the detector element size is required to be small compared to the acoustic wavelength in order to provide a near omnidirectional response. At the megahertz frequencies characteristic of PA waves this requires element sizes in the range of tens to hundreds of micrometres. It is not only challenging to fabricate piezoelectric receivers on this scale, it is also difficult to achieve adequate detection sensitivity because this scales with active area. The FP etalon sensor avoids these limitations. Element size is, to a first approximation, defined by the dimensions of the focused interrogation beam, allowing optical diffraction-limited element sizes on the scale of

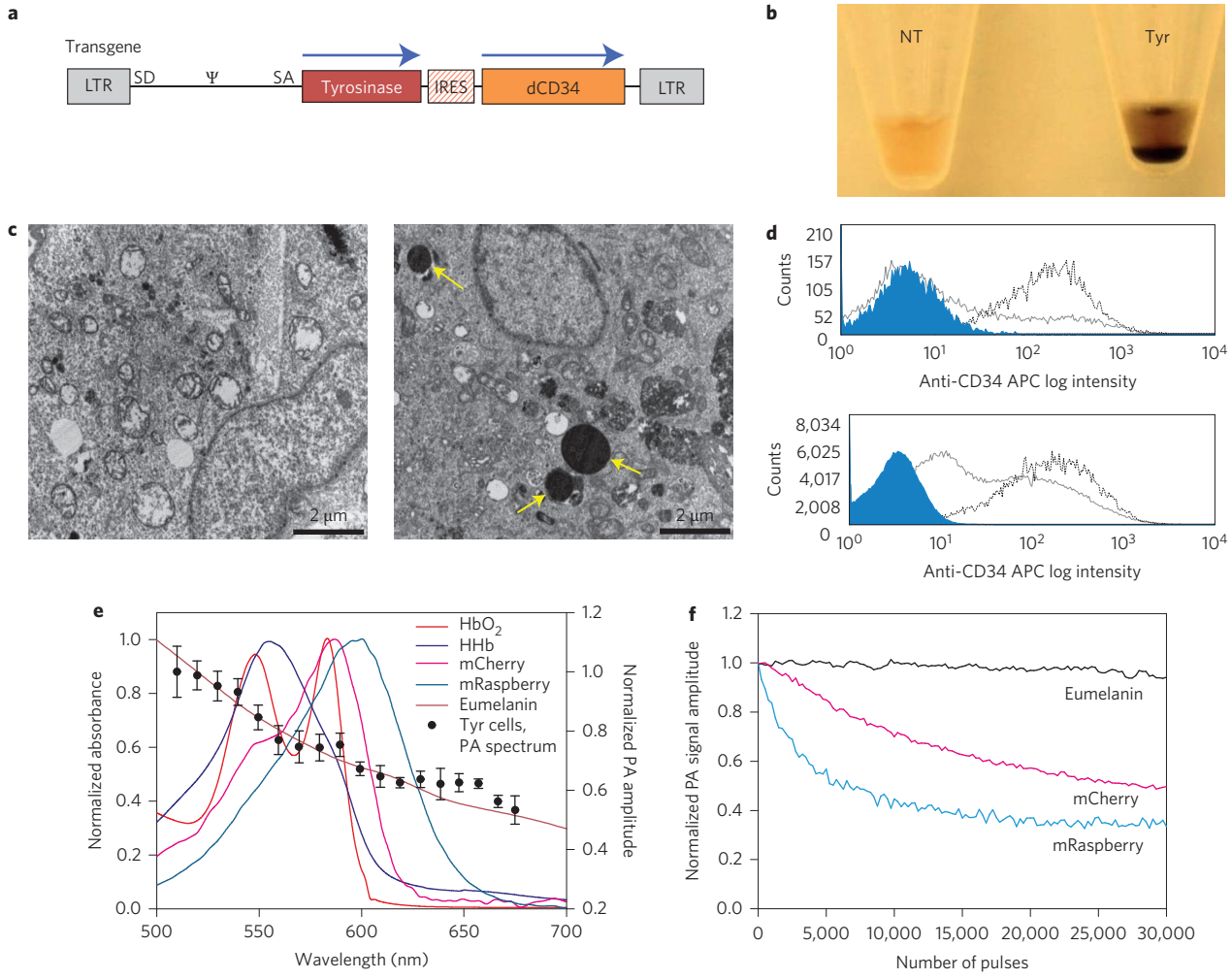

Figure 2 | Construction and *in vitro* optical and PA characteristics of Tyr-expressing cells. a, Diagram of SFG-based retroviral construct MP9883 (encoding Tyr.IRES.dCD34). Features: human tyrosinase (Tyr), internal ribosome entry site (IRES), truncated human CD34 (dCD34), long-terminal repeats (LTR). **b**, Photograph of the pigmentation of 293T cell pellets expressing Tyr. Left: non-transduced (NT); right: transduced with Tyr (Tyr). **c**, Pigmented cytoplasmic granules in cells expressing Tyr observed by TEM: NT (left) and Tyr-expressing cells (right). Magnification in both: × 5,200 (scale bars, 2 μm). Dark cytoplasmic granules larger than 1 μm in diameter were observed only in Tyr-expressing cells (yellow arrows). **d**, Flow cytometric histograms depicting the log relative expression levels of NT (blue shaded), bulk transduced cells (grey line) and cells sorted (black line) either by MACS sorting (upper histogram) or single cell cloning (lower histogram). Cells were stained with 1 μl anti-CD34 allophycocyanin (APC) antibody (BD Biosciences) and analysed by flow cytometry using a CyAn ADP analyser instrument (Beckman Coulter). **e**, PA spectroscopy of Tyr-expressing cells. The PA spectrum (filled circles) was measured in Tyr-expressing K562 cells and is overlaid with the absorbance spectrum of eumelanin (brown line) (http://omlc.org/spectra/melanin/extcoeff.html). The absorbance spectra of deoxygenated (HHb) and oxygenated (HbO_2) haemoglobin are shown in dark blue and red, respectively. The absorbance spectra of fluorescent proteins mCherry and mRaspberry are shown in pink and light blue, respectively. **f**, Photostability of eumelanin-producing cells and mCherry and mRaspberry under prolonged exposure to nanosecond laser pulses. The incident fluence was in the range 1.5–1.7 mJ cm^{-2} and the pulse repetition frequency was 50 Hz.

micrometres to tens of micrometres to be readily achieved. In addition, for this range of element dimensions, sensitivity is largely independent of the beam spot size and significantly higher than comparably sized piezoelectric receivers. For example, for the 22 μm interrogation beam spot size used in this study, the peak noise-equivalent pressure was 0.2 kPa over a 25 MHz measurement bandwidth. This is more than two orders of magnitude lower than a piezoelectric receiver of the same element dimensions and bandwidth and with similarly uniform frequency response characteristics. It is this combination of extremely small element size and high broadband detection sensitivity that provides the key acoustic performance advantage over piezoelectric detectors for high-resolution PA imaging to sub-centimetre depths.

To reconstruct a three-dimensional image from the recorded time-resolved PA signals, an image reconstruction algorithm based on time reversal was used[32,33]. With this approach, the detected signals are propagated back into the domain in time-reversed order using a numerical acoustic propagation model based on the pseudospectral time domain method. The time-reversed acoustic waves converge at a time corresponding to the incidence of the laser pulse to form a map of the initial pressure distribution; it is this map that represents the PA image. Several key pre-processing steps were undertaken (see Methods). To compensate for the low-pass filtering effect of frequency-dependent acoustic attenuation in tissue, a time-variant filter[34] was applied to the recorded PA signals. This acts to restore the more strongly attenuated high-frequency acoustic content to reduce blurring. The attenuation-compensated PA signals were then spatially upsampled by a factor of three using nearest-neighbour interpolation to reduce the disparity between the temporal and spatial sampling intervals, the latter being significantly larger than the former. This allows the computational grid used for the time-

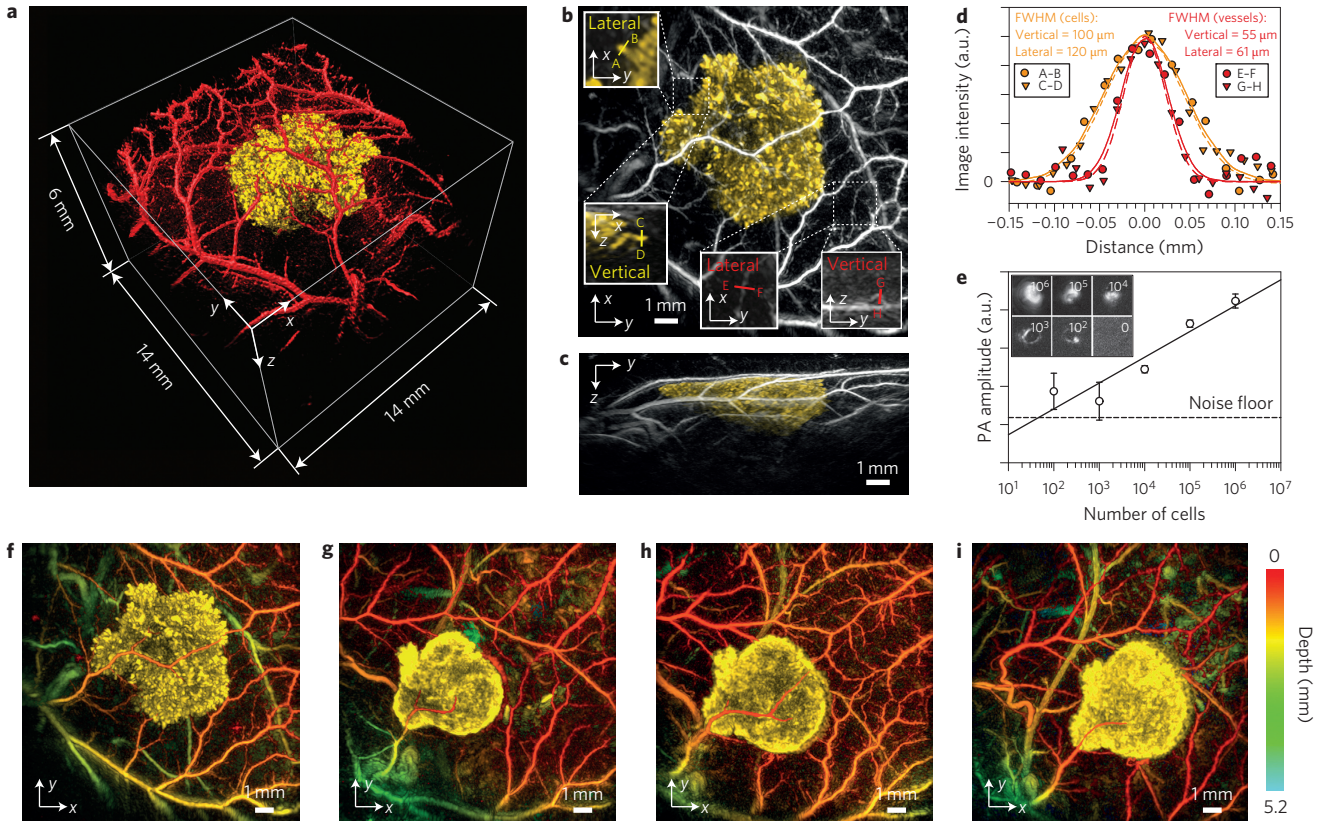

Figure 3 | *In vivo* PA images of Tyr-expressing K562 cells after subcutaneous injection into the flank of a nude mouse (λ_{ex} = 600 nm). a, Volume-rendered image (day 0); see Supplementary Movie 1 for video representation. **b**, Horizontal (*x*–*y*) MIP (day 0). **c**, Vertical (*y*–*z*) MIP (day 0). **d**, Horizontal and vertical profiles taken between the points A–B, C–D, E–F and G–H indicated in the inset figures in **b**. The FWHM of these profiles was determined by fitting a Gaussian function to the data. **e**, PA signal amplitude versus number of cells obtained by imaging increasing numbers of transduced and MACS-sorted K562 cells pelleted in tube phantoms (insets) and estimating the mean image intensity of voxels above the noise floor in each image. A linear function was fitted to the data (solid line). **f**–**i**, Serial longitudinal *in vivo* PA images (*x*–*y* MIPs) (vasculature is colour-coded for depth; K562 cells are false-coloured yellow) obtained in the same animal at different time points post-innoculation. From left to right: day 0 (**f**), day 15 (**g**), day 30 (**h**), day 52 (**i**). Images acquired at additional time points and wavelengths are provided in Supplementary Fig. 4.

reversal image reconstruction to support the full range of frequencies acquired in the temporal signals and leads to improved spatial resolution. High image fidelity also requires optimal selection of the tissue sound speed used in the time-reversal image reconstruction algorithm. This was achieved using an autofocusing approach[35] based on iteratively adjusting the sound speed and selecting the value that maximizes a sharpness metric extracted from the images reconstructed using a fast *k*-space reconstruction algorithm[36].

***In vitro* optical and PA characteristics of Tyr-expressing cells.** Although normal mammalian pigmentation arises from orchestration of a complex biosynthetic process that involves several genes[38–41] and results in the compartmentalization of eumelanin within organelles known as melanosomes[42], artificial expression of Tyr alone can also cause cellular pigmentation[43]. A retroviral vector that co-expresses Tyr and a convenient surface marker gene[44] (dCD34) was generated to allow easy engineering and selection of mammalian cells that permanently biosynthesize eumelanin (Fig. 2a). Pigmentation was observed visually in cell pellets (Fig. 2b) of a variety of cell lines when transduced by this vector. Light microscopy (Supplementary Fig. 1i–iv) revealed the formation of dark granules in cells, and transmission electron microscopy (TEM) of 293T cells showed these to be discrete cytoplasmic vesicles 1–2 μm in diameter, containing electron density rich regions (Fig. 2c and Supplementary Fig. 1v,vi). The expression of Tyr was stably maintained in long-term cultures of a variety of cell lines (Supplementary Fig. 2). Sorting of cells into homogeneously expressing populations capable of uniformly maintaining contrast was achieved by one of two methods. dCD34-expressing suspension cells were sorted using Miltenyi magnetic-activated cell sorting (MACS^R) anti-CD34 conjugated paramagnetic beads and columns. For adherent cells, single-cell clones were created by limiting dilution (Fig. 2d). The PA spectra of Tyr-expressing cells were measured by delivering laser pulses to the cell samples and recording the amplitude of the resulting PA signals as a function of wavelength using a dedicated PA spectroscopy system (see Methods and ref. 20 for details). Non-transduced (NT) cells provided no contrast, with a signal identical to that from phosphate-buffered saline (PBS) alone, whereas Tyr-expressing cells produced a strong signal-to-noise ratio (SNR). Over the wavelength range 500–700 nm, an average SNR of 18.1 was measured from 5×10^6 K562 Tyr-expressing cells pelleted in phantoms. The normalized optical absorbance spectra of synthetic eumelanin, oxyhaemoglobin (HbO_2) and deoxyhaemoglobin (HHb) are shown in Fig. 2e. Overlaid with these is the PA amplitude spectrum from cells expressing Tyr, which shows good correlation with the absorbance spectrum of eumelanin. Fluorescent proteins have been proposed as genetically encodable PA contrast agents[19], so, as an example, the absorbance spectra of redshifted fluorescent protein mCherry[45] and mRaspberry[46] are also shown. Distinct absorption of eumelanin could be detected by PAI at wavelengths extending into the near

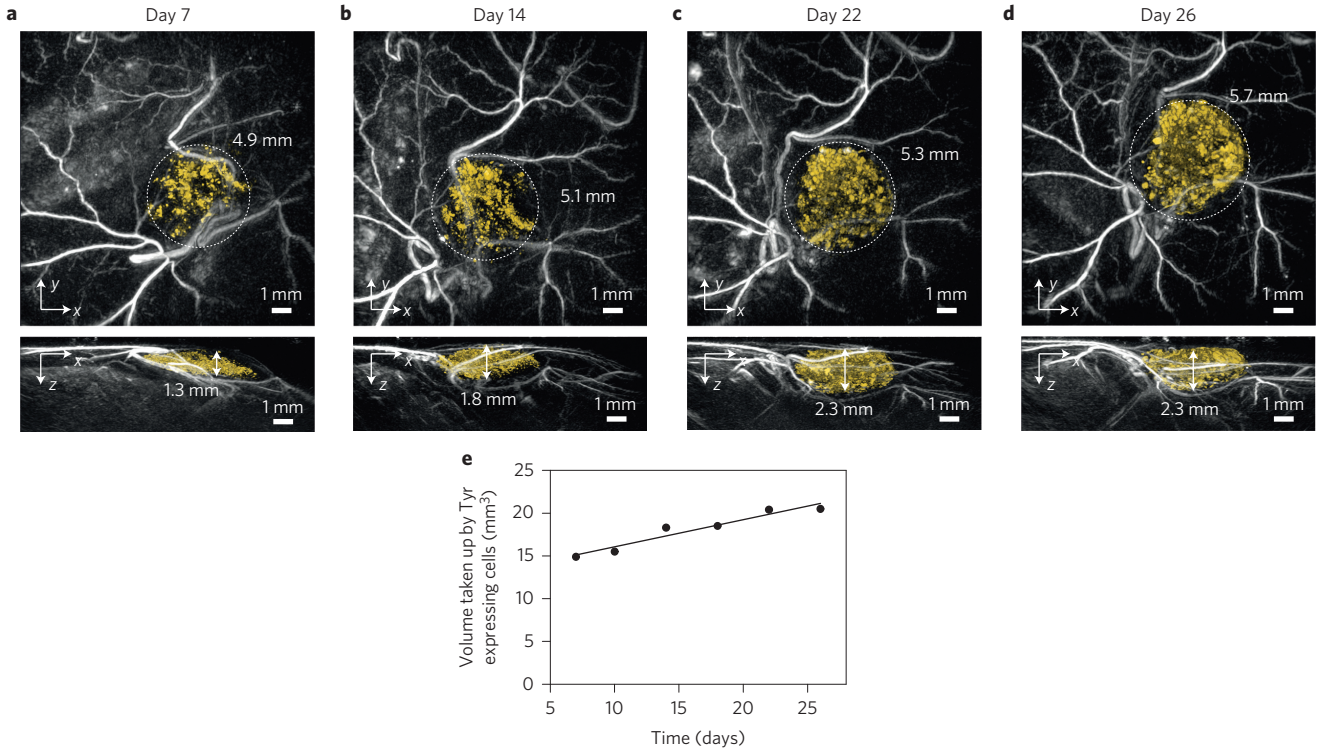

Figure 4 | *In vivo* PA images of Tyr-expressing 293T cells acquired at different times post-innoculation, illustrating cell population growth (λ_{ex} = 640 nm). **a–d**, *x–y* and *y–z* MIPs of three-dimensional image data sets acquired on day 7 (**a**), day 14 (**b**), day 22 (**c**) (see Supplementary Movie 2 for video representation) and day 26 post-innoculation (**d**) of a proliferating subcutaneous xenograft formed by 5 million 293T cells. Dashed circles around the tumour site provide an indication of the increase in diameter. See Supplementary Fig. 5 for images at additional wavelengths. **e**, Graph of volume occupied by Tyr-expressing cells versus time, illustrating cell growth of 38% over the 26 day period. A linear function was fitted to the data (solid line).

infrared (as far as 700 nm). Although the laser pulses used to generate PA signals are typically of low energy, the peak power is relatively high. This, along with total exposure times that can be up to several minutes, can cause photobleaching and other optically induced changes in certain chromophores[20]. To assess photostability, Tyr- and fluorescent protein-expressing cells were exposed to prolonged exposure of nanosecond laser pulses. The Tyr PA signal was stable when illuminated over a period of 1 h with 30,000 laser pulses at a fluence of 1.7 mJ cm^{-2}, delivered at a 50 Hz repetition rate (Fig. 2f), whereas the mCherry and mRaspberry signals were reduced to less than 60% and 40% of their original values respectively.

Longitudinal *in vivo* PAI of Tyr genetically labelled xenografts. The utility of Tyr for providing *in vivo* genetically encoded PA contrast was demonstrated in mice using K562 and 293T Tyr-expressing cells. With the former, five million anti-CD34 MACS sorted Tyr-expressing K562 cells were subcutaneously injected into the flanks of nude mice, and the xenograft was imaged at multiple wavelengths pre- and post-injection. No contrast was observed pre-injection of cells or post-injection of NT cells. Figure 3 shows PA images of K562 Tyr-expressing cells and the surrounding vasculature obtained *in vivo* using an excitation wavelength (λ_{ex}) of 600 nm. Figure 3a–c show volume-rendered and maximum intensity projection (MIP) representations of a three-dimensional image data set acquired immediately post-injection. These images show Tyr-expressing K562 cells to depths of ~4 mm with excellent contrast against the surrounding vasculature, a consequence of the high Tyr expression levels achieved and the strong optical absorption and efficient thermalization of eumelanin. The high differential contrast is particularly notable as these images were obtained at 600 nm, where blood is very strongly absorbing. Supplementary Fig. 3 illustrates the potential for achieving even greater discrimination between haemoglobin and Tyr-expressing K562 cells by imaging at longer excitation wavelengths. The two inset images on the lower right in Fig. 3b are magnified *x–y* and *y–z* MIPs of a region containing a small blood vessel at a depth of 700 µm. To obtain an approximate indication of the spatial resolution, lateral and vertical profiles (Fig. 3d) through this vessel were obtained and found to be 61 µm and 55 µm, respectively. The spatial resolution varies over the three-dimensional field of view. Based on measurements of the instrument line spread function[31] the lateral resolution at this depth (700 µm) varies from ~50 µm at the centre of the image to 65 µm at its extremities. Resolution decreases with depth due to frequency-dependent tissue acoustic attenuation and the limited aperture effect. For example, at a depth of 8 mm, the lateral resolution varies from ~100 µm at the centre of the image to 150 µm at its extremities.

The remaining two insets on the left in Fig. 3b show the locations of lateral and vertical profiles (Fig. 3d) taken through a representative cluster of cells at the periphery of the cell region. Assuming that the mean diameter of K562 cells is 11.5 µm (measured using an automated cell counter), the full-width at half-maximum (FWHM) dimensions of these profiles suggest that each of the individual clumps visible in the central cellular region in Fig. 3b corresponds to ~1,000 Tyr-expressing cells. The SNR of the above-mentioned cell cluster is 7.7, suggesting it should be possible to detect as few as 130 cells at this depth, which is broadly consistent with the *in vitro* cell detection limit indicated in Fig. 3e. The noise-equivalent eumelanin concentration of the same cell cluster is estimated to be 0.9 mM (see Methods). To demonstrate suitability for longitudinal imaging over long periods, serial *in vivo* images were obtained in the same animal at different time points up to 52 days post-injection. A selection of these images acquired at 600 nm is shown in Fig. 3f–i. Images acquired at different wavelengths over

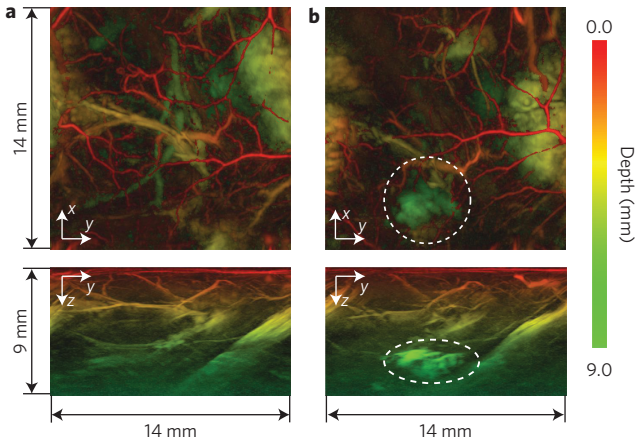

Figure 5 | Deep tissue imaging of Tyr-expressing K562 cells (λ_{ex} = 680 nm). a,**b**, *x*–*y* and *z*–*y* MIPs (colour coded for depth) of the hind leg and abdomen of a nude mouse before (**a**) and after (**b**) injection of Tyr-expressing cells below the abdominal skin and imaging through the leg. Dotted circles in the post-injection MIPs indicate the locations of the cells at a depth of up to 8 mm. See Supplementary Movie 3 for an animated volume-rendered representation of these data.

additional time points are provided in Supplementary Fig. 4. The long-lived high contrast evidenced by these results suggests that retroviral-mediated expression of Tyr provides high expression levels and is well tolerated.

Figure 4 illustrates the *in vivo* longitudinal visualization of a different cell line. In this example, a xenograft formed of Tyr-expressing 293T cells was imaged at different times over a period of 26 days. The eumelanin-based contrast provided by these cells is lower than that of the K562 cells. For this reason, at 600 nm, the cells were not visible against the strong contrast provided by haemoglobin (Supplementary Fig. 5). However, at 640 nm, the reduced absorption of haemoglobin relative to eumelanin permits unambiguous visualization of both the Tyr-expressing cells and the surrounding vasculature (Fig. 4a–d). The images also illustrate the dynamic changes over time, with xenograft growth clearly evident over the 26 day study. By segmenting the images to isolate the contrast originating from the Tyr-expressing cells, the volume occupied by the cells was determined for each time point (Fig. 4e). This shows that the xenograft volume increased by 38%, from 14.9 mm^3 to 20.5 mm^3 over a period of 26 days, illustrating the potential for visualizing cell population growth over time. Histology of the excised xenograft confirmed the presence of eumelanin (Fontana–Masson stain) and CD34 expression only in xenografts formed from Tyr-expressing cells (Supplementary Fig. 6).

Visualisation of Tyr-expressing cells at depths up to 8 mm. Because eumelanin continues to absorb light in the near-infrared, it is anticipated that it should be possible to detect Tyr-labelled cells at depths approaching 10 mm by imaging at a longer excitation wavelength. To demonstrate this, one million K562 cells were injected subcutaneously into the lower abdomen of a mouse (Fig. 5). This region was imaged at the longer wavelength of 680 nm before and after cell injection, with the mouse lying on its side so that the leg was located between the sensor and the injected cells. MIPs, colour-coded for depth, are shown in Fig. 5. The pre-injection images show the superficial vasculature of the skin (red) as well as deeper blood vessels at a depth of 3–5 mm (yellow and green). The large feature (coloured yellow/green) on the right-hand side of the *x*–*y* MIPs is part of the abdominal wall. The Tyr labelled cells are clearly visible at a depth of between 6 to 8 mm in the post-injection MIP image. For this depth range, the lateral resolution over the image area is estimated to lie between 100 μm and 150 μm.

Discussion

This study has shown that the transgenic expression of Tyr offers a viable means of achieving long-lived genetically encoded PA contrast in mammalian cells *in vivo*. The promise of this approach is underscored by several factors. First, it has been shown that Tyr-expressing cells can provide very high PA contrast over a broad range of visible and NIR wavelengths. The strong optical absorption of eumelanin beyond 650 nm where blood absorption begins to decrease is particularly advantageous as it permits discrimination against the ubiquitous endogenous contrast provided by haemoglobin. The high contrast achieved is also a consequence of the high efficiency with which eumelanin thermalizes the absorbed optical energy. This represents an important advantage over PA genetic reporters based on fluorescent proteins[19], which can exhibit low PA generation efficiency due to radiative relaxation and ground-state depopulation effects[20]. Furthermore, eumelanin exhibits significantly higher photostability than most fluorescent proteins under the high peak power pulsed irradiation typically required for efficient PA generation.

The remarkably high contrast and sensitivity that has been achieved *in vivo* is not only a consequence of the favourable optical and PA characteristics of eumelanin. It is also due to the high Tyr expression levels achieved, the signal amplification that arises from the mapping of one molecule of Tyr to multiple molecules of eumelanin and the high sensitivity afforded by the FP-based PA scanner. The combination of these factors enables Tyr-expressing cells to be visualized *in vivo* with significantly higher sensitivity and contrast, and to greater depths than previously reported[28–30]. Furthermore, the high level of contrast is achieved using single-wavelength excitation, thus avoiding the increase in acquisition time associated with multi-wavelength imaging techniques used in other studies[26,28,30]. In this study, high sensitivity was achieved with populations as low as a few tens of cells being detectable. Ultimately, single cell detection may even be possible by optimizing the choice of excitation wavelength, light delivery and detector sensitivity.

High contrast is not the sole requirement for a practical reporter gene however. Stable transduction in which the cell genome is permanently modified (so that the changes are passed to progeny cells) is essential for many practical biological applications such as visualizing cell growth. As illustrated in Fig. 4, our retroviral vector allows this to be achieved, enabling longitudinal PA visualization of an expanding cell population over long periods for the first time. Moreover, it appears to be well tolerated, as evidenced by the longevity (>7 weeks) of Tyr expression (Fig. 3). Physiologically, Tyr acts within the melanosome where pigment is sequestered. It is perhaps surprising therefore that transgenic expression of Tyr is well tolerated, alone results in pigmentation and does not appear toxic, considering the complexity of the melanogenesis within melanocyte melanosomes[42] and the toxicity of semiquinone intermediates of its biosynthesis. However, the transgene appears well tolerated. The likely explanation lies with subcellular localization motifs which act to export the enzyme to the endoplasmic reticulum and into vesicles known as endosomes where Tyr activity is confined preventing release of toxic by-products into the cell cytoplasm. Vaccinia virus-mediated Tyr expression is an alternative approach which has also been used to generate PA cellular contrast[28]. This relies upon the virus replicating in the cytoplasm outside the nucleus, without modification of the target cell genome. Contrast is therefore not transferred to daughter cells, precluding the visualization of cell growth. Furthermore, the retroviral vector used in this study exists only to modify the genome. Thereafter, its life cycle is over. Changes to the underlying cell biology due to the vector alone are therefore less

significant than those of a vaccinia virus, which needs to be actively replicating in the cytoplasm to produce tyrosinase and is thus likely to be less well tolerated over extended periods.

The approach described in this study represents an advance in the biological application of PAI. We demonstrate high-resolution three-dimensional images of genetically labelled cells at depths approaching 1 cm with unprecedented image quality, as well as the visualization of cell growth for the first time using PAI. These images cannot be obtained with comparable spatial resolution at the depths achieved using any other optical imaging modality, illustrating the potential of this approach to achieve high-resolution imaging of biological processes at the tissue, organ or even whole body level[13] in mice. We envisage a wide range of *in vivo* applications: for instance, transgenic mice could be generated that express Tyr under the control of discrete cellular promoters; transcriptional control of Tyr could facilitate its use as a biological reporter for cellular events; and the strong absorption of Tyr relative to haemoglobin beyond 650 nm makes it particularly well suited for selectively imaging transgenic tissues and microvasculature. The latter, in particular, offers new opportunities to study, for example, the dynamic interplay between cell growth and angiogenesis in cancer models. Other potential applications in cancer research include visualizing the spatial-temporal evolution of Tyr-labelled tumour cell populations in order to study tumour growth, metastasis and therapeutic response. Ultimately, the technology may also find clinical application, for example for tracking cell fate in cell-based therapies. This demonstration of the practical utility of genetically encodable contrast in deep mammalian tissues significantly extends the use of PAI as a tool for studying the biology of a wide range of disease.

Methods

Construction of human Tyr IRES CD34, production of retrovirus and cell culture. The exons of human Tyr were amplified from human genomic DNA, and the open reading frame was assembled by splicing by overlap by extension (SOE) polymerase chain reaction (PCR), and sub-cloned as an Age I/Mlu I fragment upstream of an internal ribosome entry site (IRES) and truncated CD34 (dCD34) gene in the backbone of SFG to create construct MP9883 (Fig. 1a) (NCBI accession no. 1,688,816). Plasmids encoding HA.V5.TCR alpha, mRaspberry and mCherry.I.dCD34 were previously constructed in a similar manner in our laboratory.

Retroviral vector production and transduction. Retroviral vector was generated by co-transfecting 293T cells with vector plasmid, together with RDF plasmid, which supplied the RD114 envelope (generous gift of M. Collins, UCL), and peq-pam-env, which supplied retroviral gagpol (generous gift of E. Vanin, Children's Memorial Research Center, Chicago). Supernatant was used to transduce adherent cell lines in the presence of polybrene or suspension cell lines with retronectin. Cell lines were either purchased from ATCC, or provided by the UCL Cancer Institute cell bank. The authenticity of cell lines used was assured by a digital tracking system, which provides traceability to certified cell banks. CD34 paramagnetic bead sorting was performed using anti-CD34 microbeads (Miltenyi Biotec) according to the manufacturer's protocol and single-cell clones (SSCs) were generated by limiting dilution[47]. Flow cytometry was carried out using anti-CD34 APC (BD Biosciences) or anti-dNGFR PE (Biolegend) conjugated antibodies in a CyAn instrument (Beckman Coulter). The percentage of stained cells (expressing dCD34) was used to ascertain the percentage transduction. The mean fluorescence intensity of the APC antibody was used as a measure of expression level of the gene cassette. Absorbance spectra of proteins (expressed as GST fusions and purified using GST-glutathione affinity purification) or pure melanin (Sigma Aldrich) were measured using a Varioskan Flash multimode platereader (Thermo Scientific).

PA instrumentation and *in vitro* and *in vivo* methods. The *in vitro* PA spectrum of Tyr-expressing cells was measured by varying the excitation laser wavelength and recording the peak–peak signal amplitude using an experimental arrangement similar to that described in ref. 20. Error bars in Fig. 2e represent the standard deviation of measurements obtained in three different samples. To investigate photobleaching, the amplitude of PA signals generated in Tyr-expressing cells was monitored over 30,000 laser pulses. The fluence at the sample surface was 1.5–1.7 mJ cm^{-2} depending on the wavelength, and the pulse repetition frequency was 50 Hz.

In vivo images were obtained using the imaging system which is shown in Fig. 1 and described in detail in references 10 and 31. Nude mice (MF1 Nu/Nu) anaesthetized with 1% isoflurane and oxygen (2 l min^{-1}) were injected subcutaneously with cells mixed 1:1 with Matrigel (BD Biosciences). Xenografts formed from K562 ($n = 5$) and 293T Tyr-expressing cells were imaged in a non-randomized, non-blinded study. Xenografts comprising NT cells of each type were similarly prepared to provide controls ($n = 3$), and imaged. All *in vivo* experiments were performed in accordance with the UK Home Office Animals Scientific Procedures Act (1986). The xenografts were positioned at the centre of the scan area, and aqueous gel was inserted between the skin and the FP sensor head to provide acoustic coupling. Body temperature and respiration rate were monitored and kept constant throughout the experiments. The diameter of the excitation beam incident on the skin surface was ~2 cm, and the fluence was in the range 4–7 mJ cm^{-2} depending on the wavelength, and was thus below the safe maximum permissible exposure (MPE) for skin[37]. The maximum scan area was 14×14 mm^2 and a typical scan acquired 20,000 waveforms each comprising 500 time points. The image acquisition time was 6–8 min depending on scan area and step size and was limited by the 50 Hz pulse repetition frequency of the excitation laser. The −3 dB acoustic bandwidth of the sensor was 22 MHz, the peak noise equivalent pressure was 0.2 kPa (over a measurement bandwidth of 20 MHz) and the diameter of the focused interrogation laser beam was 22 μm, which, to a first approximation, defines the acoustic element size.

Following acquisition of the PA signals, the following protocol was used to reconstruct and display the images as discussed previously. (1) To compensate for the resolution-degrading effects of acoustic attenuation, a time-variant filter was applied directly to the recorded time-domain PA signals[34]. (2) The attenuation-compensated PA signals were interpolated onto a three times finer spatial grid. (3) The tissue sound speed was estimated using an autofocus method[35]. (4) A three-dimensional image was then reconstructed from the interpolated, attenuation-compensated PA signals using a time-reversal-based algorithm[32] with the sound speed obtained in step (3) as an input parameter. The image reconstruction was implemented using k-Wave, an open-source Matlab toolbox developed at UCL for the time-domain simulation and reconstruction of PA and ultrasound wave fields (www.k-wave.org; ref. 33). (5) To aid visualization of deeper-lying features, the image intensity was normalized with respect to depth using an exponential function as a first-order correction for optical attenuation. (6) MIPs were displayed using a logarithmic image intensity scale and three-dimensional rendering, and segmentation was accomplished using Amira software (Visualization Sciences Group).

The noise-equivalent eumelanin concentration was estimated by referencing the signal obtained within the Tyr-expressing cellular region shown in the inset figures in Fig. 3b to that originating from a nearby blood vessel at the same depth and assuming a physiological haemoglobin concentration of 150 g l^{-1} and a blood oxygen saturation of 80%.

The cell detection limit data displayed in Fig. 3e were obtained by imaging five different numbers of K562 cells pelleted in tube phantoms: 10^2, 10^3, 10^4, 10^5 and 10^6 cells. The mean of the intensities of all voxels above the noise floor versus the number of cells is plotted in Fig. 3e. The noise floor was obtained by estimating the standard deviation over a localized region of the image in which there was no apparent PA signal and multiplying by a factor of three to provide the peak value. Error bars in Fig. 3e represent the standard deviation of measurements obtained in three different samples.

Segmentation of the images in Fig. 4 was undertaken to distinguish between the Tyr-expressing 293T cells and the vasculature in order to quantify the total cellular volume (Fig. 4e). The latter was estimated by selecting all voxels above the noise floor in the region of interest in the images obtained at 640 nm.

Histological analysis of *ex vivo* xenograft. Human embryonic kidney 293T and erythropoietic K562 xenografts were fixed *ex vivo* in 10% formalin (Sigma), dehydrated and paraffin-embedded for histological analysis. Samples were sectioned using a microtome (Leica RM 2135) to a thickness of 5 μm and stained for basic morphology with haematoxylin and eosin (H&E) and for eumelanin via Fontana Masson (FM), as described elsewhere. H&E staining resulted in pink cellular cytoplasmic colouration and dark purple nuclear staining, and FM staining resulted in dark brown to black colouration of eumelanin-containing cellular granules.

Antibodies and immunohistochemistry. Unless stated, all reagents, equipment and machines for immunohistochemistry were purchased from Leica Biosystems. Single immunohistochemistry was performed using a BOND-II Autostainer to stain for CD34 (clone QBEnd/10, PA0212) at dilutions of 1:20 in Novocastra Bond antibody diluent for 15 min and with an EDTA-based heat-induced epitope retrieval solution for 20 min, and detected using a bond polymer refine. Slides were dewaxed and rehydrated while on the machine, and all slides were subsequently visualized using an Axioskop 2 brightfield microscope (Zeiss).

Received 20 May 2014; accepted 26 January 2015; published online 2 March 2015

References

1. Darne, C., Lu, Y. & Sevick-Muraca, E. M. Small animal fluorescence and bioluminescence tomography: a review of approaches, algorithms and technology update. *Phys. Med. Biol.* **59,** R1–R64 (2014).
2. Branchini, B. R. *et al.* Red-emitting luciferases for bioluminescence reporter and imaging applications. *Anal. Biochem.* **396,** 290–297 (2010).

3. Jathoul, A. P., Grounds, H., Anderson, J. C. & Pule, M. A. A dual-color far-red to near-infrared firefly luciferin analogue designed for multiparametric bioluminescence imaging. *Angew. Chem. Int. Ed.* **53,** 13059–13063 (2014).
4. Ntziachristos, V. Going deeper than microscopy: the optical imaging frontier in biology. *Nature Methods* **7,** 603–614 (2010).
5. Beard, P. Biomedical photoacoustic imaging. *Interface Focus* **1,** 602–631 (2011).
6. Wang, L. V. Multiscale photoacoustic microscopy and computed tomography. *Nature Photon.* **3,** 503–509 (2009).
7. Ntziachristos, V. & Razansky, D. Molecular imaging by means of multispectral optoacoustic tomography (MSOT). *Chem. Rev.* **110,** 2783–2794 (2010).
8. Oraevsky, A. A. & Karabutov, A. A. in *Biomedical Photonics Handbook PM125* (ed. Vo-Dinh, T.) Ch. 34, 3401–3434 (CRC Press, 2003).
9. Zhang, E. Z., Laufer, J. G., Pedley, R. B. & Beard, P. C. *In vivo* high-resolution 3D photoacoustic imaging of superficial vascular anatomy. *Phys. Med. Biol.* **54,** 1035–1046 (2009).
10. Laufer, J. *et al. In vivo* preclinical photoacoustic imaging of tumor vasculature development and therapy. *J. Biomed. Opt.* **17,** 056016 (2012).
11. Laufer, J. *et al. In vivo* photoacoustic imaging of mouse embryos. *J. Biomed. Opt.* **17,** 061220 (2012).
12. Brecht, H. P. *et al.* Whole-body three-dimensional optoacoustic tomography system for small animals. *J. Biomed. Opt.* **14,** 064007 (2009).
13. Kruger, R. A., Lam, R. B., Reinecke, D. R., Del Rio, S. P. & Doyle, R. P. Photoacoustic angiography of the breast. *Med. Phys.* **37,** 6096–6100 (2010).
14. Zhang, H. F., Maslov, K., Stoica, G. & Wang, L. V. Functional photoacoustic microscopy for high-resolution and noninvasive *in vivo* imaging. *Nature Biotechnol.* **24,** 848–851 (2006).
15. De la Zerda, A., Kim, J. W., Galanzha, E. I., Gambhir, S. S. & Zharov, V. P. Advanced contrast nanoagents for photoacoustic molecular imaging, cytometry, blood test and photothermal theranostics. *Contrast Media Mol. Imaging* **6,** 346–369 (2011).
16. Luke, G. P., Yeager, D. & Emelianov, S. Y. Biomedical applications of photoacoustic imaging with exogenous contrast agents. *Ann. Biomed. Eng.* **40,** 422–437 (2012).
17. Kim, C., Favazza, C. & Wang, L. V. *In vivo* photoacoustic tomography of chemicals: high-resolution functional and molecular optical imaging at new depths. *Chem. Rev.* **110,** 2756–2782 (2010).
18. Shaner, N. C., Steinbach, P. A. & Tsien, R. Y. A guide to choosing fluorescent proteins. *Nature Methods* **2,** 905–909 (2005).
19. Razansky, D. *et al.* Multispectral opto-acoustic tomography of deep-seated fluorescent proteins *in vivo*. *Nature Photon.* **3,** 412–417 (2009).
20. Laufer, J., Jathoul, A., Pule, M. & Beard, P. *In vitro* characterization of genetically expressed absorbing proteins using photoacoustic spectroscopy. *Biomed. Opt. Express* **4,** 2477–2490 (2013).
21. Filonov, G. S. *et al.* Deep-tissue photoacoustic tomography of a genetically encoded near-infrared fluorescent probe. *Angew. Chem. Int. Ed.* **51,** 1448–1451 (2012).
22. Krumholz, A., Shcherbakova, D. M., Xia, J., Wang, L. V. & Verkhusha, V. V. Multicontrast photoacoustic *in vivo* imaging using near-infrared fluorescent proteins. *Sci. Rep.* **4,** 3939 (2014).
23. Li, L., Zhang, H. F., Zemp, R. J., Maslov, K. & Wang, L. Simultaneous imaging of a lacZ-marked tumor and microvasculature morphology in vivo by dual-wavelength photoacoustic microscopy. *J. Innov. Opt. Health Sci.* **1,** 207–215 (2008).
24. Raper, H. S. The tyrosinase-tyrosine reaction. *Biochem. J.* **21,** 89–96 (1927).
25. Paproski, R. J., Forbrich, A. E., Wachowicz, K., Hitt, M. M. & Zemp, R. J. Tyrosinase as a dual reporter gene for both photoacoustic and magnetic resonance imaging. *Biomed. Opt. Express* **2,** 771–780 (2011).
26. Krumholz, A. *et al.* Photoacoustic microscopy of tyrosinase reporter gene *in vivo*. *J. Biomed. Opt.* **16,** 080503 (2011).
27. Laufer, J. *et al.* in *Proc. SPIE, Photons Plus Ultrasound: Imaging and Sensing 2012* (eds Oraevsky, A. A. & Wang, L. V.) 82230M–82230M-5 (2012).
28. Stritzker, J. *et al.* Vaccinia virus-mediated melanin production allows MR and optoacoustic deep tissue imaging and laser-induced thermotherapy of cancer. *Proc. Natl Acad. Sci. USA* **110,** 3316–3320 (2013).
29. Qin, C. *et al.* Tyrosinase as a multifunctional reporter gene for photoacoustic/MRI/PET triple modality molecular imaging. *Sci. Rep.* **3,** 1490 (2013).
30. Paproski, R. J., Heinmiller, A., Wachowicz, K. & Zemp, R. J. Multi-wavelength photoacoustic imaging of inducible tyrosinase reporter gene expression in xenograft tumors. *Sci. Rep.* **4,** 5329 (2014).
31. Zhang, E., Laufer, J. & Beard, P. Backward-mode multiwavelength photoacoustic scanner using a planar Fabry–Perot polymer film ultrasound sensor for high-resolution three-dimensional imaging of biological tissues. *Appl. Opt.* **47,** 561–577 (2008).
32. Treeby, B. E., Zhang, E. Z. & Cox, B. T. Photoacoustic tomography in absorbing acoustic media using time reversal. *Inv. Prob.* **26,** 115003 (2010).
33. Treeby, B. E. & Cox, B. T. k-Wave: MATLAB toolbox for the simulation and reconstruction of photoacoustic wave fields. *J. Biomed. Opt.* **15,** 021314 (2010).
34. Treeby, B. E. Acoustic attenuation compensation in photoacoustic tomography using time-variant filtering. *J. Biomed. Opt.* **18,** 036008 (2013).
35. Treeby, B. E., Varslot, T. K., Zhang, E. Z., Laufer, J. G. & Beard, P. C. Automatic sound speed selection in photoacoustic image reconstruction using an autofocus approach. *J. Biomed. Opt.* **16,** 090501 (2011).
36. Koestli, K. P., Frenz, M., Bebie, H., Weber, H. P. & Köstli, K. P. Temporal backward projection of optoacoustic pressure transients using Fourier transform methods. *Phys. Med. Biol.* **46,** 1863–1872 (2001).
37. *British standard safety of laser products* (BS EN 60825-1) edn 1.2, August (2001).
38. Calvo, P. A., Frank, D. W., Bieler, B. M., Berson, J. F. & Marks, M. S. A cytoplasmic sequence in human tyrosinase defines a second class of di-leucine-based sorting signals for late endosomal and lysosomal delivery. *J. Biol. Chem.* **274,** 12780–12789 (1999).
39. Berson, J. F., Harper, D. C., Tenza, D., Raposo, G. & Marks, M. S. Pmel17 initiates premelanosome morphogenesis within multivesicular bodies. *Mol. Biol. Cell* **12,** 3451–3464 (2001).
40. Tachibana, M. *et al.* Ectopic expression of MITF, a gene for Waardenburg syndrome type 2, converts fibroblasts to cells with melanocyte characteristics. *Nature Genet.* **14,** 50–54 (1996).
41. Kuzumaki, T., Matsuda, A., Wakamatsu, K., Ito, S. & Ishikawa, K. Eumelanin biosynthesis is regulated by coordinate expression of tyrosinase and tyrosinase-related protein-1 genes. *Exp. Cell Res.* **207,** 33–40 (1993).
42. Raposo, G. & Marks, M. S. Melanosomes-dark organelles enlighten endosomal membrane transport. *Nature Rev. Mol. Cell Biol.* **8,** 786–797 (2007).
43. Bouchard, B., Fuller, B. B., Vijayasaradhi, S. & Houghton, A. N. Induction of pigmentation in mouse fibroblasts by expression of human tyrosinase cDNA. *J. Exp. Med.* **169,** 2029–2042 (1989).
44. Fehse, B. *et al.* CD34 splice variant: an attractive marker for selection of gene-modified cells. *Mol. Ther.* **1,** 448–456 (2000).
45. Shaner, N. C. *et al.* Improved monomeric red, orange and yellow fluorescent proteins derived from *Discosoma* sp. red fluorescent protein. *Nature Biotechnol.* **22,** 1567–1572 (2004).
46. Wang, L., Jackson, W. C., Steinbach, P. A. & Tsien, R. Y. Evolution of new nonantibody proteins via iterative somatic hypermutation. *Proc. Natl Acad. Sci. USA* **101,** 16745–16749 (2004).
47. Hafler, D. A. *et al.* Oligoclonal T lymphocytes in the cerebrospinal fluid of patients with multiple sclerosis. *J. Exp. Med.* 167, 1313–1322 (1988).

Acknowledgements

This work was funded by the UK Biotechnology Research Council (BBSRC) grant no. BB/I014357/1. Additional funding was provided by the gene-therapy division of the UK NIHR University College London Hospital Biomedical Research Centre. This work was also supported by King's College London and University College London Comprehensive Cancer Imaging Centre, Cancer Research UK and the Engineering and Physical Sciences Research Council (EPSRC), in association with the Medical Research Council and Department of Health, UK, and European Union project FAMOS (FP7 ICT, contract no. 317744). P.B. is funded by an EPSRC Leadership Fellowship and J.L. is funded by an ERC starting grant (281356). The authors thank J. Paterson (UCL Advanced Diagnostics) for assistance with immunohistochemistry, K. Venner for assistance with transmission electron microscopy (TEM) and C. Futter for assistance in interpreting the electron micrographs. H. Dortay (TU Berlin) is thanked for helpful comments on the manuscript and P. Varga (AO Research Institute Davos, Switzerland) for assistance with the use of Amira.

Author contributions

A.J. carried out molecular cloning, cell preparation, maintenance and analysis, animal work, the design of experiments, *in vitro* characterizations and *in vivo* photoacoustic imaging, and assisted with preparation of the manuscript. J.L. undertook the photoacoustic spectroscopy and imaging studies, the reconstruction, processing and analysis of the *in vivo* images, and assisted with preparation of the manuscript. O.O. contributed to tissue phantom experiments and implemented the cell detection limit study. B.T. and B.C. developed the signal processing, image reconstruction and visualization methods. E.Z. designed and constructed the photoacoustic scanner. P.J. provided cell lines, and helped with *in vitro* and *in vivo* imaging and histological analyses. A.P. helped with analysis of cells by flow cytometry and with the general experimental design. RBP carried out the production of virus, and helped with cellular analyses and the use of different iterations of his novel marker gene. T.M. performed immunohistochemistry. M.L. was responsible for invocation of the project, and contributed to experimental planning, motivation, the use of facilities and equipment, experimental focus and editing of the manuscript. R.B. provided cell lines, mice, microscopy and the use of the Home Office Project Licence. M.P. provided gene and vector designs, codon optimization, experimental designs, and directed the overall focus of the work and writing of the manuscript. P.B. directed the photoacoustic imaging component of the project and organized and co-wrote the manuscript.

Additional information

Supplementary information is available in the online version of the paper. Reprints and permissions information is available online at www.nature.com/reprints. Correspondence and requests for materials should be addressed to P.B.

Competing financial interests

The authors declare no competing financial interests.